A sensitivity analysis on parameters that affect a multi-step material decomposition for spectral CT

Nathaniel R. Fredette, Amar Kavuri, Mini Das

Nathaniel R. Fredette, Amar Kavuri, Mini Das, "A sensitivity analysis on parameters that affect a multi-step material decomposition for spectral CT," Proc. SPIE 10573, Medical Imaging 2018: Physics of Medical Imaging, 105734K (9 March 2018); doi: 10.1117/12.2294956

SPIE.

Event: SPIE Medical Imaging, 2018, Houston, Texas, United States

A sensitivity analysis on parameters that affect a multi-step material decomposition for spectral CT

Nathaniel R. Fredette[1], Amar Kavuri[1] and Mini Das[1,2,*]

[1]Department of Biomedical Engineering, University of Houston, Houston, TX 77204, USA
[2]Department of Physics, University of Houston, Houston, TX 77204 USA

ABSTRACT

When using a photon counting detector (PCD) for material decomposition problems, a major issue is the low-count rate per energy bin which may lead to high image-noise with compromised contrast and accuracy. We recently proposed a multi-step algorithmic method of material decomposition for spectral CT, where the problem is formulated as a series of simpler and dose efficient decompositions rather than solved simultaneously. While the method offers higher flexibility in the choice of energy bins for each material type, there are several aspects that should be optimized for effective utility of these methods. A simple domain of four materials: water, calcium, iodine and gold was explored for testing these. The results showed an improvement in accuracy with low-noise over the single-step method where the materials were decomposed simultaneously. This paper presents a comparison of contrast-to-noise ratio (CNR) and retrieval accuracy in both single-step and multi-step methods under varying acquisition and reconstruction parameters such as Wiener filter kernel size, pixel binning, signal size and energy bin overlap.

Keywords: Material decomposition, Spectral CT, Photon counting detectors, Sensitivity analysis

1. INTRODUCTION

Photon counting spectral detectors have the potential to be used in several applications requiring tissue discrimination and quantitation such as breast imaging[1-2], characterization of arterial plaques[3-4], quantification of liver iron overload[5-6], quantification of bone mineral density[7], kidney stone composition analysis[8] and phase contrast imaging[9,10]. Separating the total counts into multiple energy bins however leads to low count data sets with reduced signal to noise and accuracies in material decomposition. In order to effectively improve the utility of counts in each acquired data bin, we recently proposed a multi-step material decomposition method which breaks the decomposition problem into a series of steps where the most informative energy bins or bin combinations are chosen rather than solving the system simultaneously with all of the acquired data[11]. The method works by grouping similar materials in earlier steps thereby virtually reducing the number of unknowns in each step. Once a given material is retrieved in the earlier steps, this forms part of the data for subsequent steps thereby making the problem better conditioned in subsequent steps. Successful decomposition of up to six materials (as seen in Fig. 1) is presented using eight energy bins and comparison with single-step approach is demonstrated.

In this paper, we examine the capabilities and limitations of this method as it comes to a few parameters that affect material decomposition. First, we are interested in seeing how filtering influences material decomposition results. There are many filter types, but we chose the Wiener filter as it is an empirical filter that attempts to model the noise in the data. It is not an edge-preserving filter though, so rounding of edges is apparent in the decomposition results. Second, we are interested in the effects of binning pixels in the projection domain prior to reconstruction on resulting decomposition accuracies and noise properties. The study examines if the noise reduction due to averaging neighboring pixels is reflected in these image domain material decomposition techniques. Third, we are interested in capturing the trends in the decomposition results as signal size is varied. This study attempts to understand the limits of decomposition as it pertains to signal size for a common pixel and voxel size. Finally, it is of interest to determine the effect of collecting data with overlapping versus separated energy bins on material decomposition. This study tries to capture the ideal collection conditions as it comes to energy bin positions and widths. The Cramer Rao Lower Bound (CRLB) can be employed to capture theoretical limits on decomposition results as has been shown in other studies and this metric will be employed in future studies[6,12-14]. The digital phantom used in this study has signal and background properties that could emulate a breast imaging like problem with contrast materials. However, the results of parameter selection may have wider applications.

Medical Imaging 2018: Physics of Medical Imaging, edited by Joseph Y. Lo, Taly Gilat Schmidt, Guang-Hong Chen, Proc. of SPIE Vol. 10573, 105734K
 · doi: 10.1117/12.2294956

The energy-resolved data was simulated at every keV from one to the tube peak voltage. Equal count bins were then defined by dividing the simulated x-ray energy spectrum into eight and the data at each keV was then summed into these bins. Poisson noise was then added to the binned data so that the data would have suitable statistics.

2. METHODS

The parameters investigated in this study were filtering kernel size, binning, signal size and energy bin overlap. These parameters were varied, and results of material decomposition were quantified using the existing single-step method[11] and the new multi-step method[11]. The single-step method (described by Eqn. 1) states that the total attenuation of an object, $\mu_{total}(\vec{r}, E_j)$, is comprised of the sum of the attenuations of each of its constituent materials, $\mu_i(E_j)$, multiplied by their respective geometric volume fraction distribution, $f_i(\vec{r})$, as seen in Eqn. 1 where r is the spatial variable, E_j represents energy bin j and i represent the material index. Previously, the single-step method and the first step of the multi-step method were implemented in projection domain. For simplicity, all steps of both methods are now implemented in reconstruction space even though the method can be applied completely in either domain.

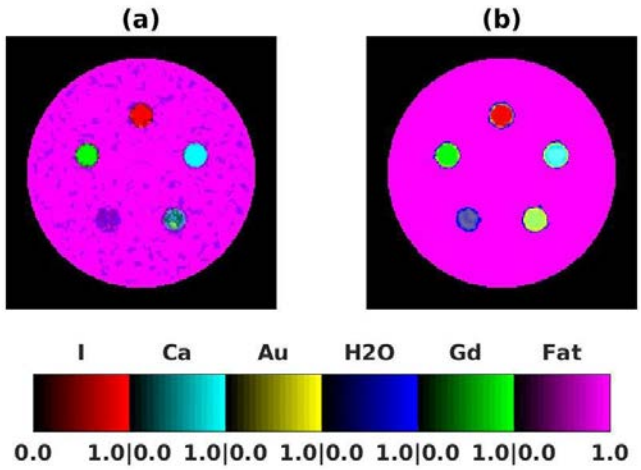

Figure 1: Color coded (a) single-step (left) and (b) multi-step (right) decomposition results for the six-material problem.

$$\mu_{total}(E_j, \vec{r}) = \sum_{i=1}^{M} \mu_i(E_j) f_i(\vec{r}) \tag{1}$$

We propose that the material decomposition can now be computed in a series of steps each separating one new material from the measured intensity data. The materials are separated by how distinct the material is from the other materials based on the linear attenuation versus energy curves. In our problem, this means that the background material, water, is separated from the attenuation data containing four materials first. Next, the K-edge contrast agent material iodine is separated from the remaining data of three materials because of its unique discontinuity at 33 keV. Third, the next most attenuating material of calcium is separated. Finally, a refinement step is used to separate the last material of gold.

The first step of the four material, material decomposition problem can be seen in Eqn. 2 where the linear attenuation coefficients of the low attenuating elements are combined, and the volume fraction of the mixture is represented. In this step, we assume that the linear attenuation coefficients of the low attenuating materials are similar enough that they can be represented by the average of the two materials or $\bar{\mu}_{3,4}(E_j)$. The index j indicates the median energy of the bin from the acquired multi-bin data of a spectral detector forming our first system of equations.

$$\mu_{total}(E_j, \vec{r}) = \mu_1(E_j) f_1(\vec{r}) + \mu_2(E_j) f_2(\vec{r}) + \bar{\mu}_{3,4}(E_j)\, \bar{f}_{3,4}(\vec{r}) \tag{2}$$

In our model problem, material 1 represents water, material 2 represents iodine, material 3 represents calcium and material 4 represents gold. The least squares solution to Eqn. 2 with reconstructed multiple energy bin intensity data (obtained using a PCD) yields volume fractions of $f_1(\vec{r})$, $f_2(\vec{r})$ and the average of $f_3(\vec{r})$ and $f_4(\vec{r})$. Here materials 3 and 4 are lumped to mimic a material with average material properties. While we can also obtain $f_2(\vec{r})$ from the prior solution, we seek to reformulate the problem, thereby enabling further iterations to yield better solutions of $f_2(\vec{r})$, $f_3(\vec{r})$ and $f_4(\vec{r})$ which form signals in this problem. In the second step, the problem is reformulated to separate the K-edge material of iodine from the remaining three material mixture as represented in Eqn. 3. The same assumption about the similarity of calcium and gold is made in this step as well.

$$\mu_{total}(E_j, \vec{r}) - \mu_1(E_j) f_1(\vec{r}) = \mu_2(E_j) f_2(\vec{r}) + \bar{\mu}_{3,4}(E_j)\, \bar{f}_{3,4}(\vec{r}) \tag{3}$$

In implementing the least squares solution to this equation, one assumes the knowledge of the water map obtained from step 1 as a prior information as shown on the left-hand side of Eqn. 3. The solution yields a map of material 2 (iodine)

and a map of a material that mimics a combination of materials 3 and 4, which is discarded when proceeding to the next step. In step 3, the problem is reformulated again to separate the next most attenuating material of calcium from the remaining two material mixture as represented in Eqn. 4.

$$\mu_{total}(E_j,\vec{r}) - \mu_1(E_j)f_1(\vec{r}) - \mu_2(E_j)f_2(\vec{r}) = \mu_3(E_j)f_3(\vec{r}) + \mu_4(E_j)f_4(\vec{r}) \quad (4)$$

In the final step, the last material, gold, is refined to improve the accuracy of the decomposition of this material in Eqn. 5.

$$\mu_{total}(E_j,\vec{r}) - \mu_1(E_j)f_1(\vec{r}) - \mu_2(E_j)f_2(\vec{r}) - \mu_3(E_j)f_3(\vec{r}) = \mu_4(E_j)f_4(\vec{r}) \quad (5)$$

At each step, the respective equation (Eqn. 2, 3, 4 or 5) is solved using multiple energy bin data collected via the initial, single acquisition with a PCD. The same data can be reformulated in later steps to reduce the number of bins and increase count statistics. Using the conservation of volume assumption, the system of energy based equations (based on Eqns. 2, 3, 4 and 5) can be used to solve for material volume fractions using a weighted bounded variable least-squares approach.

Percent errors, CNRs and noise standard deviations (NSDs) were computed for each of the materials in both single step and multi-step decomposition. Percent errors were computed for the single and multi-step decomposition techniques via Eqn. 6 where $f_{ROI,i}$ and $f_{ROI,i,true}$ indicate the calculate and true volume fractions in ROI i, respectively.

$$Error_{ROI,i} = \frac{|f_{ROI,i} - f_{ROI,i,true}|}{f_{ROI,i,true}} \times 100 \quad (6)$$

The CNR calculations were conducted for the single and multi-step decomposition techniques using the relationship in Eqn. 7 where $\sigma^2_{ROI,i}$ and $\sigma^2_{RestOfImage}$ indicate the calculated variances in the volume fractions in ROI i and the rest of the image, respectively.

$$CNR = \frac{|f_{ROI,i} - f_{RestOfImage}|}{\sqrt{\sigma^2_{ROI,i} + \sigma^2_{RestOfImage}}} \quad (7)$$

The NSDs were computed for the single and multi-step decomposition techniques using the relationship seen in Eqn. 8 where $\sigma_{ROI,i}$ is the standard deviation in the volume fractions of the voxels in ROI i.

$$NSD_{ROI,i} = \sigma_{ROI,i} \times 100 \quad (8)$$

3. RESULTS AND DISCUSSION

In all cases, a four-material cylindrical digital phantom model was generated with three contrast wells embedded. The phantom is 2cm diameter of water with 2mm signals of calcium, iodine and gold. A depiction of the four-material model can be seen in Fig. 2 (a). The x-ray energy spectrum is depicted in Fig. 2 (b) with the nominal choice of energy bins overlaid. The material linear attenuation curves for the four materials versus energy with the nominal energy bins overlaid is shown in Fig. 2 (c). The concentrations of calcium, iodine and gold in the model were 140mg/mL, 18mg/mL and 8mg/mL, respectively. The x-ray energy spectrum was divided into eight equal count bins that define the nominal energy bins chosen for this study. A 120kVp spectrum was used and the x-ray spectrum was filtered by 1.68mm of aluminum. A total dose of 7.92mGy was distributed over 360 projections measured over a 360-degree arc. A CdTe detector was simulated with a sensor thickness of 1.0mm and eight energy bins. The nominal detector pixel size was 110X110 micron squared. The nominal reconstruction voxel size was 118.75X118.75X118.75 micron cubed. The filtered back projection (FBP) method was used for reconstructing the projection data into 3D images. Color-coded qualitative results of single and multi-step decomposition for the nominal four-material problem can be seen in Fig. 3 for reference. It can be noticed that single-step method fails to decompose the gold region accurately and the multi-step technique does much better. For all other cases, the maximum percent error out of the four ROIs seen in Fig. 2 (a) is reported for the single and multi-step techniques. The value of the true volume fractions in each of the ROIs is 1.0 and this was used in the percent error and CNR calculations. The maximum NSD of all four ROIs was reported for each simulation as this should provide the worst case. The average of the CNRs of all ROIs was computed for the decomposition techniques to provide a description of the CNRs for all regions.

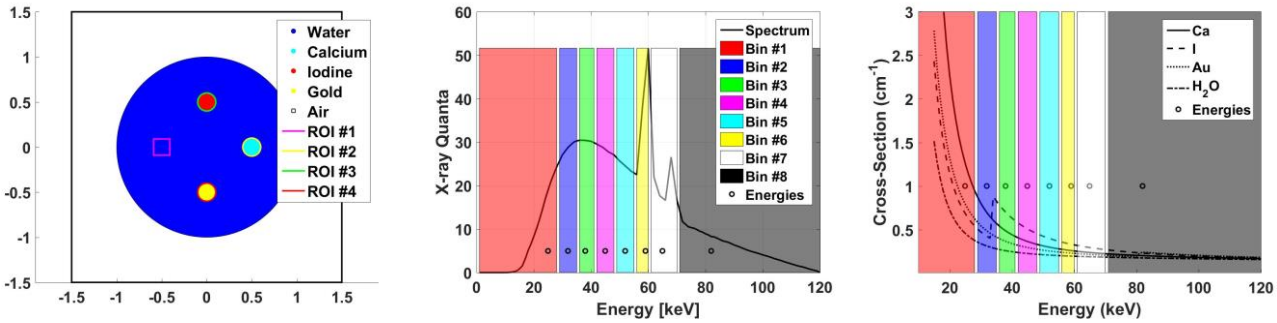

Figure 2: (a) Layout of materials for the four-material model. (b) 120 kVp x-ray source spectrum divided into eight equal count energy bins based on the flat field. The baseline representative energies used in the material decomposition are shown as open circles. (c) Attenuation curves for calcium, iodine, gold and water with energy bins and representative energy values used to calculate the model linear attenuation coefficients used in material decomposition.

3.1 Filtering

The effects of filtering in the projection domain were explored with a Wiener filter of differing kernel sizes. The goal was to determine the effects of noise reduction in the projection domain via a common filter on material decomposition. It is expected that there is a sweet-spot in the amount of filtering due to the kernel size where noise is sufficiently reduced while edges are maintained, and this study aimed to find it. In all cases, the projection data was generated based on simulations of the four-material model represented in Fig. 2 with 110μmX110μm pixels. Poisson noise was added and then the noisy projections were filtered using differing kernel size Wiener filters. These kernel sizes were 1X1 (no filter), 3X3, 5X5, 7X7, 9X9 and 11X11. The filtered projections were then reconstructed using filtered back projection to a voxel size of 118.75μmX118.75μmX118.75μm. Material decomposition was then calculated using the single and multi-step methods and the results can be seen in Fig. 4. The maximum decomposition errors increased with increasing kernel size. Therefore, filtering with a small kernel Wiener filter yielded the best results. This is because the Wiener filter introduces more rounding of edges as the kernel size increases and this rounding decreases accuracies. However, because of the much greater accuracy of the multi-step method, the CNR of the multi-step technique vastly outperforms the single-step technique. This can be attributed to the iterative operations leading to non-linearities in multi-step and energy bin optimization that are performed. The single-step method has lower noise for higher kernel dimensions than the multi-step technique. The noise in multi-step can build up as the noisy volume fraction results from earlier steps are used in later steps in the decomposition. But overall, the multi-step technique outperforms single-step as seen in the lower errors and higher CNRs.

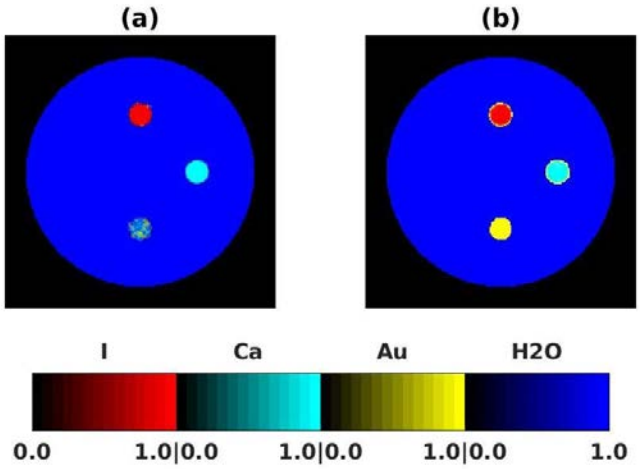

Figure 3: Color coded (a) single-step (left) and (b) multi-step (right) decomposition results for the nominal four-material problem.

3.2 Binning

The effects of binning the projection data from smaller to larger pixels before reconstruction versus acquiring data with larger pixels directly on material decomposition were investigated. This study attempts to understand if the noise in the projections can be improved by combining every four pixels (through averaging) thereby improving the pixel statistics over the baseline where no binning is performed. To test this, projection data was generated from 4-material models based on Fig. 2 with five different pixel sizes of 55μmX55μm, 110μmX110μm, 220μmX220μm, 440μmX440μm and 880μmX880μm. The data with the four smallest pixels sizes was then binned in a 2X2 fashion. The four binned datasets and the four larger pixel size datasets were then reconstructed to slightly larger voxels of

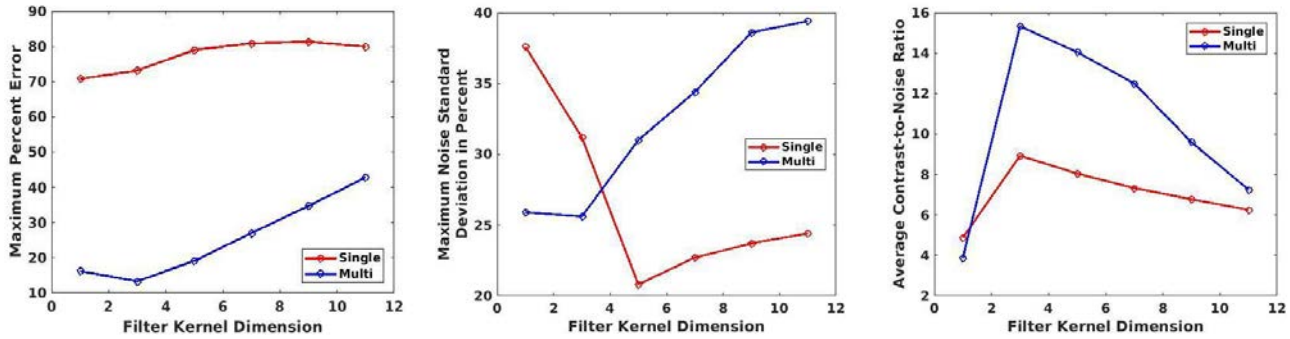

Figure 4: Filtering effects on material decomposition examined through single and multi-step decomposition techniques. (a) Displays the maximum percent errors, (b) displays the maximum NSDs and (c) displays the average CNRs of the four material regions.

118.75μmX118.75μmX118.75μm, 237.5μmX237.5μmX237.5μm, 475μmX475μmX475μm and 950μmX950μmX950μm via filtered back projection. The single and multi-step material decompositions were then performed on both datasets. Images with equivalent effective voxels sizes were then compared and the results can be seen in Fig. 5. The maximum errors generally increase as the effective voxel size increases. This is effectively a sampling problem as fewer voxels are used to represent a material region as voxels size increases leading to a higher fraction of the total voxels in the region capturing the transition between materials and resulting in lower accuracies. Acquiring data with larger pixels directly generally produces decomposition results with lower errors, but the errors are very similar for the two decomposition methods. The large peak in the CNRs for the multi-step technique can be attributed to a nearly zero variance in the water region of the water map. This CNR was capped at 100.0 for the sake of plotting but was much larger and is due to the thresholding performed after the first step of multi-step material decomposition. The NSDs for the single and multi-step methods are similar except for the larger effective voxel sizes. However, these large voxel size images had very few voxels making the images low in quality and less practical for a real imaging task. Overall, single and multi-step decomposition show similar performance in terms of binning as displayed in the percent errors and CNRs.

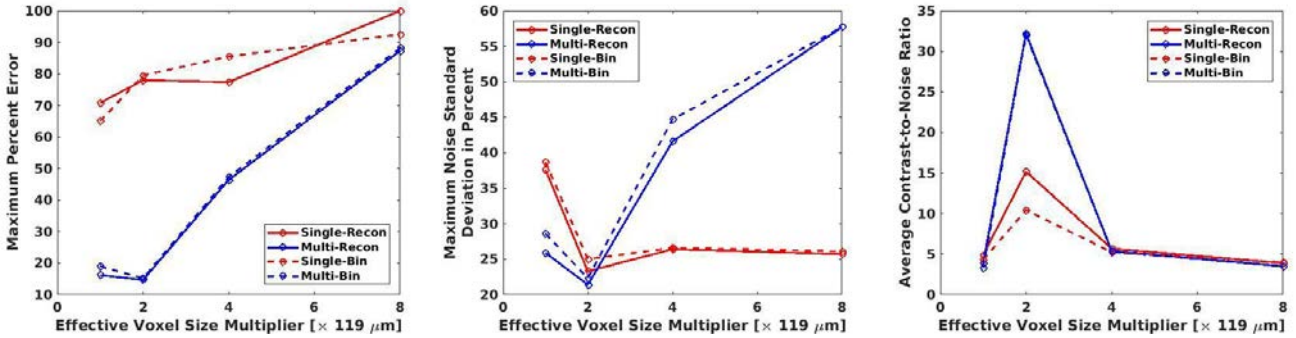

Figure 5: Binning effects on material decomposition examined through single and multi-step decomposition techniques. (a) Displays the maximum percent errors, (b) displays the maximum NSDs and (c) displays the average CNRs of the four material regions. "Recon" denotes a larger pixel acquisition where as "Bin" denotes a smaller pixel acquisition with binning.

3.3 Signal size

Next, the effects of signal size on material decomposition were explored. It is expected that there is a spatial resolution limit for the modeled 110μmX110μm pixel size detector for a 7.92mGy measurement and it is desired to explore this limit with respect to material decomposition. Therefore, four-material models based on Fig. 2 were constructed with varying signal sizes of 0.5mm, 1.0mm, 2.0mm, 3.0mm, 4.0mm, 5.0mm and 6.0mm. These models were used to generate projection data and then this data was reconstructed using filtered back projection. Material decomposition was then performed using single and multi-step decomposition techniques. The decomposition results for the differing signal size problems can be seen in Fig. 6. As the signal size increases, the error tends to decrease, and the standard deviation tends to remain relatively constant. However, the error changes very little for signal sizes of 1.0mm and above indicating that this may be the limiting size for this pixel size and dose combination. The reason for this trend can be explained again by sampling as signal size increases more voxels lie within the material region leading to a more accurate representation of the mean in the region. This trend is more evident in the errors of the multi-step method as the single-step results tend to flatten off. This is because

the noise in the gold region of the gold material map (as seen in Fig. 3) is much more prominent in the single-step technique and limits the accuracy of the decomposition. The attenuation properties of 8mg/mL of gold are the most similar to water of the decomposed materials making it the most difficult to distinguish. The single-step NSDs remain rather flat indicating that noise and signal size are independent. The decrease in NSD as signal size increases for multi-step can be explained again by the thresholding operations in multi-step. If the accuracy increases and the noise remains the same (as indicated by single-step), then the thresholding in multi-step becomes more effective as more voxels lie on the correct side of the thresholds. The CNRs decrease as this signal size increases. This is probably due to the slight increase in noise in the signal and background regions as the signals become larger. Again, thresholding and flexibility in the choice of number and location of energy bins used in the multi-step method allow for CNRs greater than single-step. The maximum CNR for the multi-step technique seen for the 1.0mm signal size occurs because the noise in the water region is nearly zero for this case. The CNR for this case was 133.7. If the simulation was run again with different noise, these decomposition results may change resulting in a smaller CNR. The multi-step method clearly out performs single-step as evidenced by the lower maximum errors and higher average CNRs for all signal sizes.

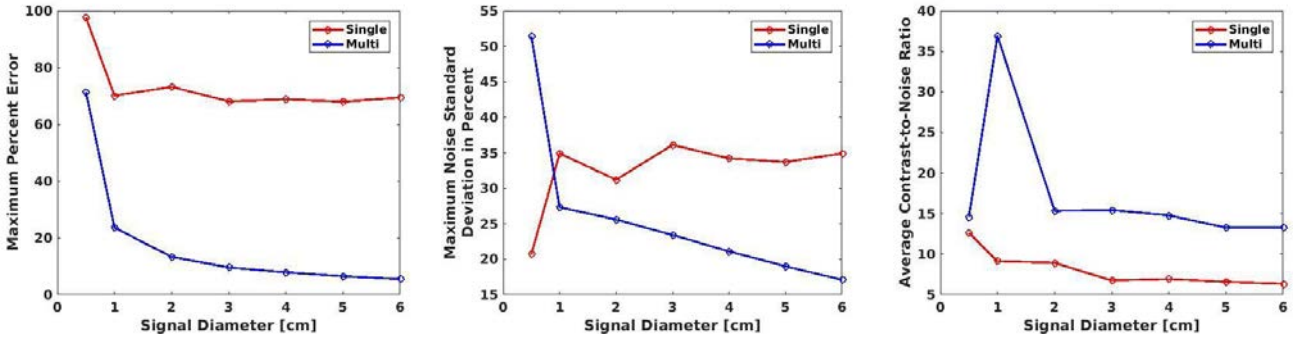

Figure 6: Signal size effects on material decomposition examined through single and multi-step decomposition techniques. (a) Displays the maximum percent errors, (b) displays the maximum NSDs and (c) displays the average CNRs of the four material regions.

3.4 Energy bin overlap

Finally, the effects of energy bin overlap or spacing on material decomposition were explored. As the bins become wider and overlap more, each bin becomes less unique from its neighbor and the system becomes more underdetermined. As the bins become narrower with greater spacing, bins are more unique, but count statistics get worse. So, it was desired to discover this trade-off and find an optimal configuration. The energy-resolved data was generated with equal width bins with 1keV spacing (-1keV overlap) as [9,22], [23,36], [37,50], [51,64], [65,78], [79,92], [93,106] and [107,120] keV, respectively. Additional four-material models based on Fig. 2 were constructed with varying amounts of overlap of -9keV, -5keV, -1keV, 1keV, 5keV, 9keV, 13keV, 17keV, 21keV, 25keV and 29keV. These projection datasets were then reconstructed using FBP and decomposition using both techniques was performed. Energy weighting based on the signal-to-noise ratio (SNR) of each region of the data was used in the multi-step decomposition and weighting based on the SNR of the water region was used for single-step decomposition[15]. The decomposition results for the differing amounts of energy bin overlap can be seen in Fig. 7. Increasing the overlap generally decreases the decomposition errors until 17keV for single-step and 5keV for multi-step. Therefore, it seems that some overlap can successfully improve photon statistics without creating too much data redundancy. The errors are much larger for single-step. The multi-step CNR exceeds the single-step CNRs for all amounts of overlap. The sharp peaks in the multi-step CNRs can again be attributed to nearly zero variance in the water region after thresholding. These variances may change with different noise realizations. Single-step has lower NSDs than multi-step and this is again due to the propagation of noise from step to step in multi-step. The noise for both material decomposition methods generally decreases as the bins become wider and overlap increases. The multi-step method clearly out performs single-step as evidenced by the lower maximum errors and higher average CNRs for all amounts of energy bin overlap.

4. CONCLUSIONS

The effects of filtering, binning, varying signal sizes and varying amounts of energy bin overlap were studied to explore the capabilities and limitations of the single and multi-step decomposition techniques. Although the NSDs for single-step are often lower than those of multi-step, the vast improvement in accuracy achieved by the multi-step method allowed for greater CNRs than single-step. This is due to steps in the decomposition process that introduce non-linearities

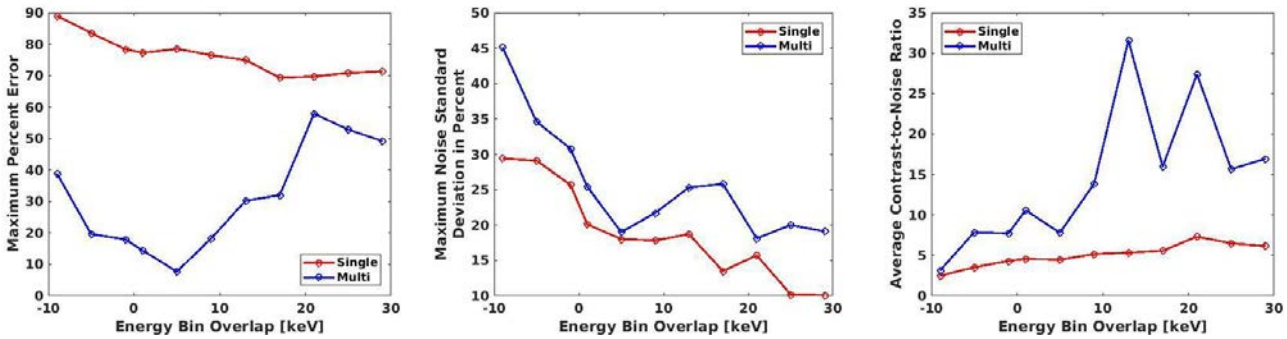

Figure 7: Energy bin overlap effects on material decomposition examined through single and multi-step decomposition techniques. (a) Displays the maximum percent errors, (b) displays the maximum NSDs and (c) displays the average CNRs of the four material regions. In these graphs, negative overlap indicates that the energy bins were separated by the given amount.

such as thresholding and energy bin optimization. Material specific weighting in multi-step material decomposition based on SNR to overcome measured attenuation data with unequal statistics was demonstrated in the energy bin overlap study. This preferential weighting based on the material being decomposed in a multi-step approach provides the method with even more flexibility not available in the single-step approach and resulted in low percent errors and high CNRs. And overall, the multi-step method consistently outperformed the single-step technique for the problems analyzed herein. Future simulations will include a realistic breast phantom with realistic breast texture and material properties. The problem will be examined in both projection domain and reconstruction domain decomposition. Furthermore, this method will be tested with bench top PCD based CT system using a CdTe detector. These results will be presented at the conference.

ACKNOWLEDGEMENTS

This work was partially supported by funding from the US Department of Defense (DOD) Congressionally Directed Medical Research Program (CDMRP) Breakthrough Award BC151607 and the National Science Foundation CAREER Award 1652892.

REFERENCES

[1] Le, H. Q., Molloi, S., “Segmentation and quantification of materials with energy discriminating computed tomography: A phantom study,” Med. Phys. 38(1), 228–237 (2011).
[2] Lee, S., Choi, Y., Kim, H., “Quantitative material decomposition using spectral computed tomography with an energy-resolved photon-counting detector,” Phys. Med. Biol. 59(18), 5457–5482 (2014).
[3] Alessio, A. M., MacDonald, L. R., “Quantitative material characterization from multi-energy photon counting CT,” Med. Phys. 40(3), 031108–1 – 031108–8 (2013).
[4] Ronaldson, J. P., Zainon, R., Scott, N. J. A., Gieseg, S. P., Bulter, A. P., Butler, P. H., Anderson, N. G., “Toward quantifying the composition of soft tissues by spectral CT with medipix3,” Med. Phys. 39(11), 6847–6857 (2012).
[5] Mendonca, P. R. S., Lamb, P., Sahani, D. V. “A flexible method for multi-material decomposition of dual-energy CT images,” IEEE Trans. Med. Imag. 33(1), 99–116 (2014).
[6] Li, Z., Leng, S., Yu, L., Yu, Z., McCollough, C. H., "Image-based material decomposition with a general volume contraint for photon-counting CT.," Proc. SPIE 9412, 94120T (2015).
[7] Yu, L., Liu, X., McCollough, C., “Pre-reconstruction three-material decomposition in dual-energy CT,” Proc. SPIE 7258, 72583V (2009).
[8] Schmidt, T. G., Petkas, F., “Region-of-interest material decomposition from truncated energy-resolved CT,” Med. Phys. 38(10), 5657–5666 (2011).
[9] Gursoy, D., Das, M., “Single-step absorption and phase retrieval with polychromatic x rays using a spectral detector,” Optics Letters 38(9), 1461-1463 (2013).
[10] Das, M., Liang Z., “Spectral x-ray phase contrast imaging for single-shot retrieval of absorption, phase, and differential-phase imagery,” Optics Letters 39(21), 6343-6346 (2014).
[11] Fredette, N., Lewis, C., Das, M., “A multi-step method for material decomposition in spectral computed tomography,” Proc. SPIE 10132, 101321C (2017).
[12] Roessl, E., Brendel, B., Schloma, J. P., Thran, A., Proska, R., “Sensitivity of photon-counting K-edge imaging dependence on atomic number and object size,” Proc. IEEE NSS, 4016-4021 (2008).

[13] Roessl, E. and Herrmann, C., "Cramer-Rao lower bound of basis image noise in multiple-energy x-ray imaging," Phys. Med. Biol. 54(5), 1307-1318 (2009).
[14] Modgil, D., Rigie, D. S., Wang, Y., Xiao, X., Vargas, P. A. and La Riviere, P. J., "Material identification in x-ray microscopy and micro CT using multi-layer, multi-color scintillation detectors," Phys. Med. Biol. 60(20), 8025-8045 (2015).
[15] Schmidt, T. G., "Optimal "image-based" weighting for energy-resolved CT," Med. Phys. 36(7), 3018-3027 (2009).